Polygonal Meshes of Highly Noisy Images based on a new Symmetric Thinning Algorithm with Theoretical Guarantees

Mohammed Arshad Siddiqui[1][a] and Vitaliy Kurlin[2][b]
[1]*PDPM Indian Institute of Information Technology Design and Manufacturing, Jabalpur, India*
[2]*University of Liverpool, United Kingdom*
MohdSiddiqui@iiitdmj.ac.in, Vitaliy.Kurlin@liverpool.ac.uk

Keywords: edge detection, thinning, skeletonization, polygonal mesh

Abstract: Microscopic images of vortex fields are important for understanding phase transitions in superconductors. These optical images include noise with high and variable intensity, hence are manually processed to extract numerical data from underlying meshes. The current thinning and skeletonization algorithms struggle to find connected meshes in these noisy images and often output edge pixels with numerous gaps and superfluous branching point. We have developed a new symmetric thinning algorithms to extract from such highly noisy images 1-pixel wide skeletons with theoretical guarantees. The resulting skeleton is converted into a polygonal mesh that has only polygonal edges at sub-pixel resolution. The experiments on over 100 real and 6250 synthetic images establish the state-of-the-art in extracting optimal meshes from highly noisy images.

1 INTRODUCTION

Microscopic image analysis of topological defects (called *quantum vortices*) in symmetry-breaking phase transitions is now a hot topic in cosmology and high-temperature superfluids and superconductors (Lin et al., 2014). Figure 1 shows a piezo-response force microscopic image of a vortex field. The underlying vortex field is a complicated mesh of non-convex polygons that is hard to recognize even by human experts because of the highly variable noise.

To understand phase transitions, physicists urgently need to count various statistics of vortex fields such as the number and positions of vertices, the number and sizes of polygonal domains. Since past algorithms produced incomplete meshes with discontinuities or hanging endpoints, see section 6, human experts had to manually count features of vortex images. This paper automates the collection of statistical data that will enable a discovery of high-temperature superconductors as motivated in (Lin et al., 2014).

Definition 1. *A* vortex mesh *on an image* Ω *is a skeleton or an embedded graph splitting* Ω *into domains with polygonal edges that consist of straight line segments and meet at vertices of degree at least 3.*

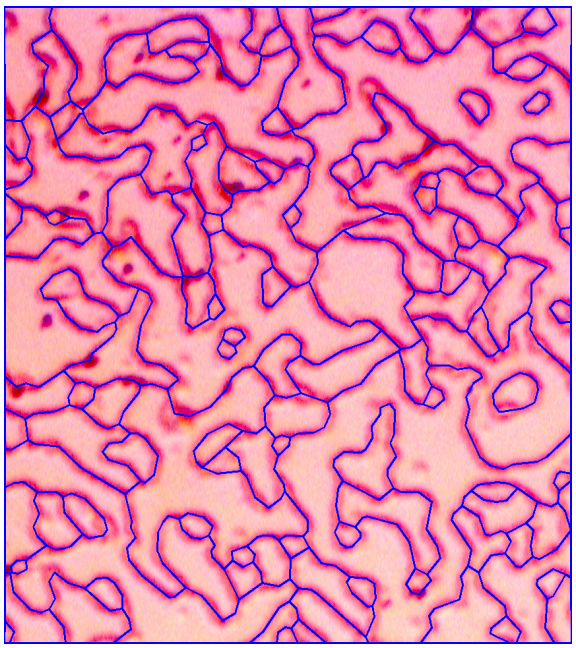

Figure 1: Our new mesh on top of a typical microscopic image, see high resolution images in supplementary materials.

Optimal Mesh Problem. For any highly noisy vortex image as in Figure 1, find a connected polygonal mesh that minimizes the average intensity (to get a darkest skeleton) and has a minimum number of vertices.

[a] https://orcid.org/0000-0002-9747-3132
[b] https://orcid.org/0000-0001-5328-5351

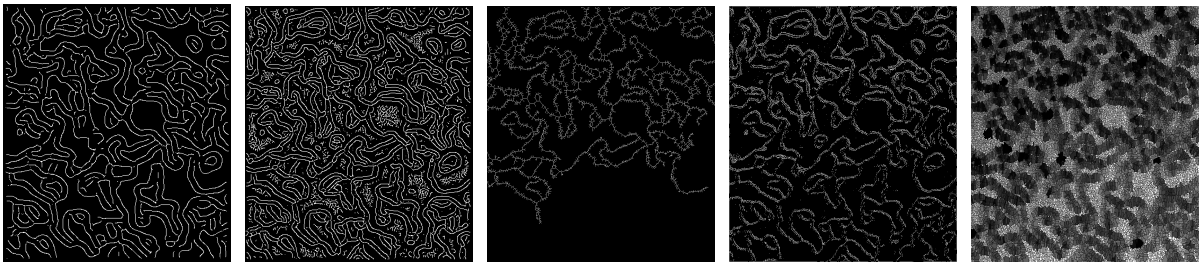

Figure 2: Past edge detection on the input in Figure 1. **1st**: many disjoint components based on a small number of Canny edge pixels (Canny, 1986). **2nd**: many superfluous components based on a large number of Canny edge pixels. **3rd**: fuzzy logic skeletonization (Kamani et al., 2018). **4th**: (Asghari and Jalali, 2015). **5th**: watershed by (Soille and Vincent, 1990).

The primary minimization is for the average intensity, because the underlying vortex mesh is represented by darker pixels. The secondary minimization is for the number of degree 2 vertices to simplify polygonal lines between higher degree vertices.

Here are the challenges in solving the above problem for the highly noisy microscopic images in practice.

• Polygonal lines have a large and variable thickness and can meet at higher degree vertices at any angle.

• The intensity largely varies and leads to many noisy edges, compare with a ground truth in Figure 18.

• Microscopic images often contain isolated noisy blobs that should be ignored and also larger blobs that should be treated as vertices or parts of lines.

Here are the novelty and contributions of the paper. to the state-of-the-art skeletonization of noisy images.

• New Definition 5 formalizes a 1-pixel wide skeleton guaranteed in the output by Theorem 6.

• The new erosion algorithm in section 4 preserves the homotopy type (stronger than a graph connectivity) for any binary image, see Definition 3, Theorem 8.

• Table 1 in section 6 shows that our thinning outperforms all past algorithms on the minimum average intensity on over 100 real images and also produces simpler meshes without erroneous degree 1 vertices.

• Table 2 has standard accuracy measures averaged over 6250 ground truths and shows that the new symmetric thinning in section 5 is robust under noise.

Here is the pipeline for the optimal mesh extraction.

Stage 1: the Otsu thresholding (Otsu, 1979) is adapted for microscopic images with variable noise in section 3 to get a connected binary image.

Stage 2: any binary image is symmetrically thinned to a 1-pixel wide skeleton without degree 1 vertices, see proofs of Theorems 6 and 8 in section 4.

Stage 3: a 1-pixel wide skeleton from Stage 2 is converted to a mesh whose polygonal lines are further straightened for a statistics analysis in section 6.

2 A REVIEW OF PAST WORK

Edge detection algorithms. The Canny edge detector (Canny, 1986) depends on 3 thresholds and can output many disjoint components, see Figure 2.

Morse-Smale skeleton (Delgado-Friedrichs et al., 2014) consists of gradient flow curves joining local extrema and saddle points of the grayscale intensity. Figure 3 shows a Morse-Smale skeleton with many superfluous black vertices joined by white curves.

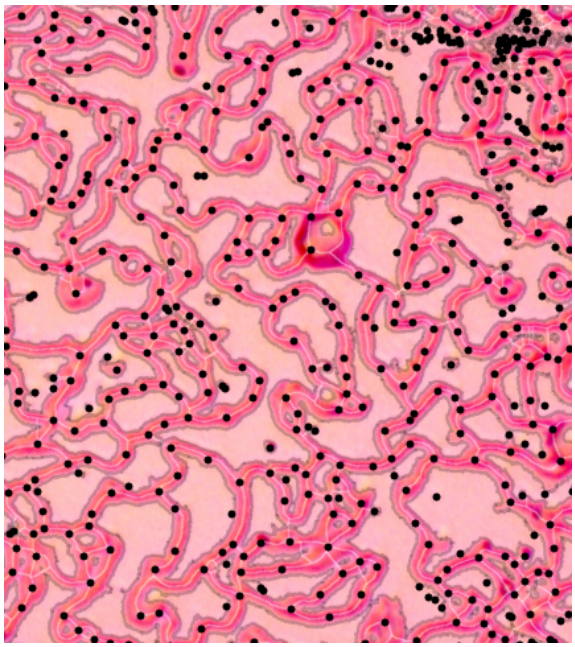

Figure 3: The Morse-Smale skeleton (Delgado-Friedrichs et al., 2014) with black dots for local minima and saddles.

The recent survey on skeletonization (Saha et al., 2016) is a comprehensive review of past approaches and current challenges. Typical requirements for a skeleton representing a binary (black-and-white) image is (1) centrality, (2) invariance under rotations and other deformations, (3) connectedness or preservation

of a topological type (Kurlin, 2015a), (Kurlin, 2015b), (Kalisnik et al., 2019), (Smith and Kurlin, 2019).

Another aim from Bernard in (Bernard and Manzanera, 1999) is to guarantee that a skeleton is 1-pixel wide, because a big block of black pixels such as (Saha et al., 2016, Figure 1) or Figure 11 is an obstacle for many thinning algorithms. The new thinning algorithm in sections 4-5 solves problem by introducing a 1-pixel wide skeleton in Definition 5.

OpenCV offers the thinning by (Zhang and Suen, 1984) and (Guo and Hall, 1989). Both methods use a 3×3 neighborhood to decide which pixels to remove. The first method (Zhang and Suen, 1984) consists of two sub-iterations where the pixels are removed from north-east and south-west corners, then from the south-east and north-west corners. The similar second method guarantees (Guo and Hall, 1989, Proposition A.3) the global connectivity of clusters, not the homotopy type in Definition 3, so a circular cluster can become a non-closed polygonal line.

Fuzzy logic: Kamani (Kamani et al., 2018) proposed a skeletonization method based on fuzzy logic, which can take any grayscale image, see Figure 2(3).

CNNs: convolutional neural networks (Wang et al., 2018), (Shen et al., 2017), (Panichev and Voloshyna, 2019) were particularly successful in cases when a lot of ground truth data is available, see Fig. 4.

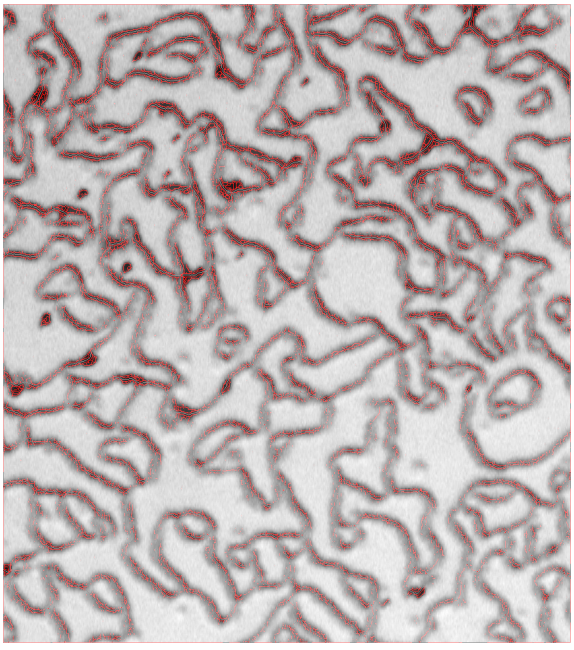

Figure 4: The output by (Asghari and Jalali, 2015) on the image from Figure 1. One could zoom in and find many disjoint components instead of one big connected skeleton.

3 The new adaptive thresholding

This section discusses Stage 1 of the proposed solution to the Optimal Mesh Extraction Problem from section 1. Since a mesh is still detectable by human eye in grayscale, the mesh problem was stated in terms of minimizing the average grayscale intensity. Stage 1 will build a connected binary image.

Definition 2. *For a given width w and height h, a* binary *image on the continuous domain $\Omega = [0,w] \times [0,h] \subset R^2$ is a set of black unit square pixels whose complement in Ω consists of the white unit square pixels in the background. An image I is* connected *if the union of its black pixels forms a connected sub-graph in the 8-connected grid of Ω.*

We have tried many thresholdings to get a connected image that can be further thinned. Our microscopic images have uneven illumination with darker regions towards the image boundary. This gradual change in intensity was not uniform in given images. The global and local thresholding methods (Bernsen, 1986), (Niblack, 1985), (Phansalkar et al., 2011), (Sauvola and Pietikäinen, 2000), (Soille, 2013) often fail to preserve continuity of edges in the noisy image from Figure 1, see outputs of above binarizations in Figure 6. The clustering-based thresholding (Otsu, 1979) couldn't find an optimal threshold. Figure 5 shows the Otsu thresholding with many components.

To resolve uneven illumination, we find optimal parameters for Otsu binarization in sub-images of size $M \times M$ within 2584×1936 images. Otsu binarization chooses an optimal threshold using the histogram of all intensities. Since some sub-images are dark, we shift any intensity i lower than a certain bound b for all sub-images by $i \mapsto (i+b)/2$.

The parameters M and b are dynamically selected for each image as follows. The original image is divided into $M \times M$ sub-images whose average intensities are calculated. The value of M increases from 50 to 400 in increments of 25. We choose M so that the standard deviation of the average intensity in sub-images is minimal. Then b is set as the average intensity of the optimal sub-image. This shift implicitly increases the optimal Otsu threshold and yields a connected binary image in Figure 5 (middle).

A resulting image can have small holes as in the middle of Figure 5, green box. Physicists advised us that expected domains have at least 50 pixels, so we have filled all small holes as in the right picture of Figure 5, instead of the persistence-based hole detection (Kurlin, 2014b), (Kurlin, 2014a), (Kurlin, 2016). The output of Stage 1 in Figure 5 (right) has few small black components, which are removed in sections 4-5.

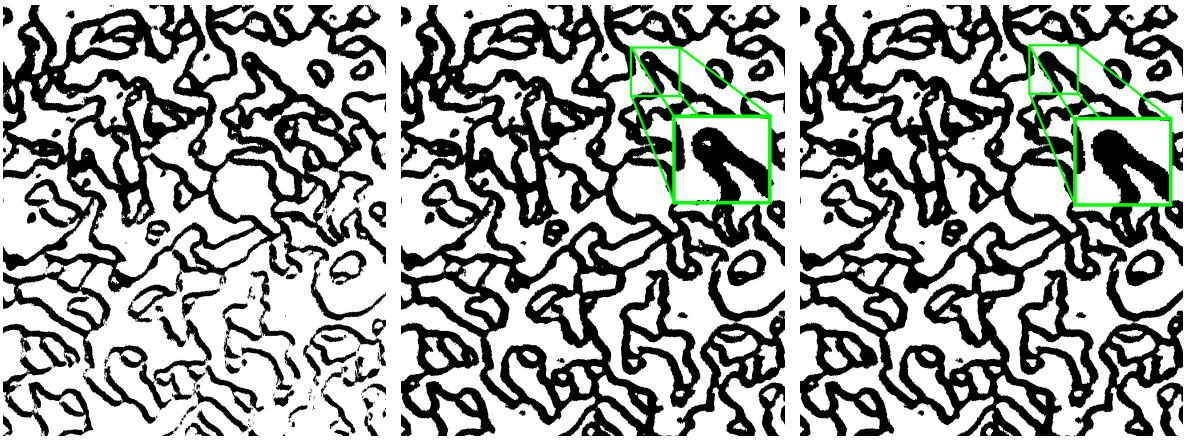

Figure 5: **Left**: original Otsu thresholding (Otsu, 1979) breaks connectivity in Figure 1. **Middle**: the new adaptive thresholding outputs a better connected image, compare the bottom parts. **Right**: output of Stage 1 after filling small holes.

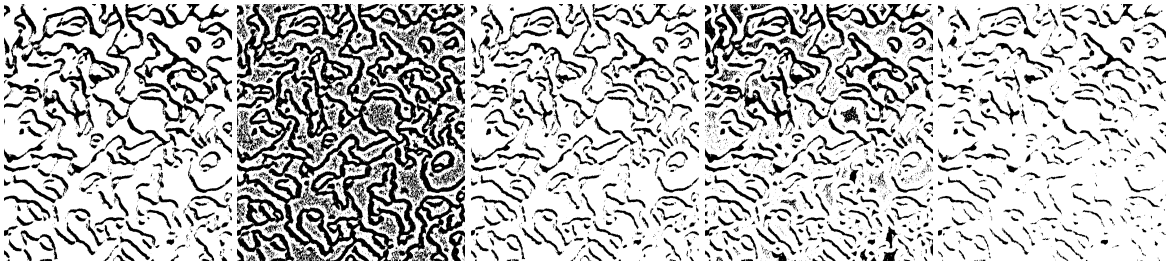

Figure 6: Outputs of several local thresholding methods on the input image in Figure 1. **1st**: (Bernsen, 1986), **2nd**: (Niblack, 1985), **3rd**: (Phansalkar et al., 2011), **4th**: (Soille, 2013) and **5th**: (Sauvola and Pietikäinen, 2000).

4 The new erosion with guarantees

The output of Stage 1 is a binary image that covers polygonal lines of a required vortex mesh. The next stage is to thin (or erode) the binary image to preserve its homotopy type without making any holes.

Definition 3. *A* subimage *of a binary image I consisting of black pixels on a continuous domain Ω is a subset $J \subset I$ of black pixels considered on the same domain Ω of I. A* homotopy *(or a* deformation retraction*) $f : I \to J$ is a continuous family of functions $f_t : \Omega \to \Omega$, $t \in [0,1]$, such that $f_0 = \mathrm{id}_\Omega$, $f_1 = f$ and all f_t keep the points of J fixed.*

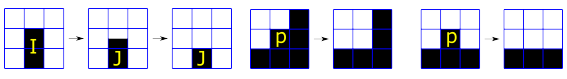

Figure 7: A homotopy of an image I to its subimage J is a continuous deformation.

Figure 8: Examples of Erosion 2 when we remove a pixel p with two changes of colors in neighbors from Definition 4.

A homotopy can be visualized as a sequence of pixel removals that preserve the topological shape of a binary image. A removal of a pixel with only one neighbor (in the 3×3 neighborhood) is a homotopy by Definition 3. A removal of a pixel whose two neighbors become disconnected (as formalized in Definition 4) cannot be realized by a continuous family of deformations, so isn't a homotopy.

Definition 4. *(neighbors) Any non-boundary black (foreground) pixel p has* 8 neighbors *in the* 3×3*-neighborhood. Any white (background) pixel has only* 4 neighbors*. When we walk around the pixel p (say, clockwisely starting from any neighbor), we count the number of* color changes *in the 8 neighbors of p from black to white and from white to black.*

Section 5 describes the new algorithm that symmetrically removes pixels starting from an external layer and outputs a better skeleton with a lower average intensity. We now discuss a simpler thinning when pixels are removed one by one being processed from top to bottom and from left to right.

Erosion 1. Remove a black pixel that has at most 1 neighbor, e.g. any isolated pixel is removed as an outlier. We remove pixels with 1 neighbor as in Figure 7 since a vortex mesh has no degree 1 vertices.

Erosion 2. Remove a black pixel p if colors change twice around p, see Definition 4 and Figure 8.

Erosion 3. Remove a black pixel p if p has 4 changes of colors, but all its neighbors are pairwise adjacent to each other in the 8-connected grid, see Figure 9.

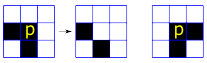

Figure 9: Erosion 3 removes a pixel p with four changes of colors. in neighbors.

Figure 10: Erosion 4 removes a pixel p when all black neighbors are connected.

Erosion 4. We remove a black pixel p if p wasn't removed by any of Erosions 1-3, p has at least two white neighbors and all its black neighbors form a connected sub-graph (in the 8-connected grid), see Figure 10. This erodes busy junctions as in Figure 11 (right), which were obstacles for homotopy-preserving thinning (Saha et al., 2016). Erosion 3 was separated from Erosion 4 to speed up the algorithm.

The erosion algorithm scans a binary image row by row, processing black pixels in each row from left to right. Black pixels are stored in a map-structure for quick access by a pixel position. For any black pixel, we try Erosions 1,2,3,4 in this order until all remaining pixels cannot be removed by Erosions 1-4.

New Erosion 4 resolves busy junctions to get a 1-pixel wide skeleton (see Theorem 6) and keeps the homotopy type of a binary image (modulo 1-pixel holes) due to Theorem 8. Theorems 6 and 8 are two 'edges of the thinning sword' justifying wider applications of the thinning based on Erosions 1-4.

Definition 5. *A binary image I consisting of black pixels is called a* 1-pixel wide skeleton *if any 2×2 block contains at most 3 black pixels of I except the case in Figure 11 (left), where each of 4 black pixels has a diagonal neighbor.*

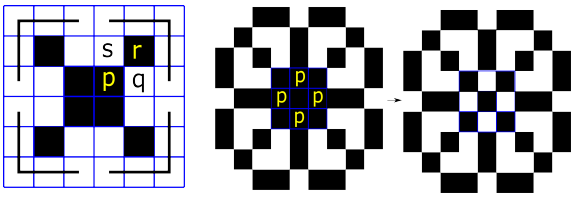

Figure 11: **Left**: the 2×2 block cannot be removed because of 4 diagonal neighbors. **Right**: Erosion 4 removes 4 pixels p in the previously unresolved junction (Saha et al., 2016).

The diagonal neighbors in Figure 11(left) might be kept by Erosions 1-4 if each of 4 black corner lines contains at least one black pixel. Figure 11(right) shows the power of new Erosion 4, which can penetrate big black blocks by creating only 1-pixel holes that can be later filled if needed. Our microscopic images had no superfluous 1-pixel holes from Erosion 4.

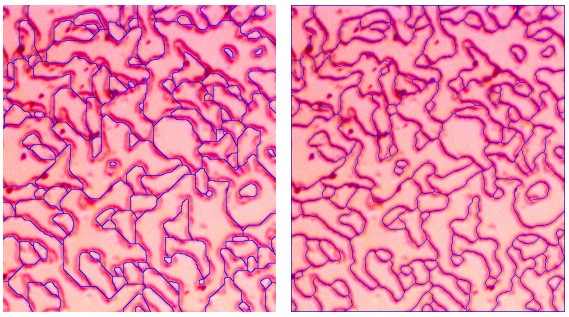

Figure 12: Ablation study: past thinning vs symmetrical. **Left:** too straight lines after erosion in section 4. **Right:** more accurate polygonal lines after symmetric thinning.

Theorem 6. *For any binary image I with fixed boundary black (background) pixels, the algorithm based on Erosions 1-4 outputs a 1-pixel wide skeleton.*

Proof of Theorem 6. If I isn't a 1-pixel wide skeleton, we can find a 2×2 block B of black pixels adjacent (by a side) to at least one white pixel q. The side neighbor $p \in B$ of q cannot be removed by Erosion 4 only if its side neighbor s is white and corner neighbor r is black as in the left picture of Figure 11 so that r becomes disconnected from other neighbors of p if q is eroded. The other 3 pixels in B cannot be eroded only if they have diagonal neighbors in Figure 11. □

Definition 7. *A* 1-pixel hole *in a binary image I of black pixels is a white pixel sharing 4 sides with black pixels, see the central white pixel in the last picture of Figure 10. A connected component C of an image I is* trivial *if C has no holes larger than 1-pixel holes.*

Theorem 8. *For any image I without trivial components and 1-pixel holes, the erosion after filling 1-pixel holes outputs a subimage homotopic to I.*

Proof of Theorem 8. If a central black pixel p shares a side with a white pixel, the removal of p is realized by a homotopy in the sense of Definition 3, see Figure 7. If p is eroded and the 4 neighbors sharing sides with p are black, Erosion 4 was applied and p becomes a 1-pixel hole by Definition 7. Erosions 1-4 preserve the local connectivity, i.e. the neighbors of p remain connected in the 8-connected grid.

Each of the 4 side neighbors q of p in Figure 10 cannot be later eroded, otherwise the two corner black pixels (sharing sides with p and corners with q) become disconnected in the 3×3 neighborhood of q. Hence p will keep all its 4 side neighbors and will remain a 1-pixel hole that will not affect the homotopy type (after filling 1-pixel holes in J). □

5 Symmetric thinning and a mesh

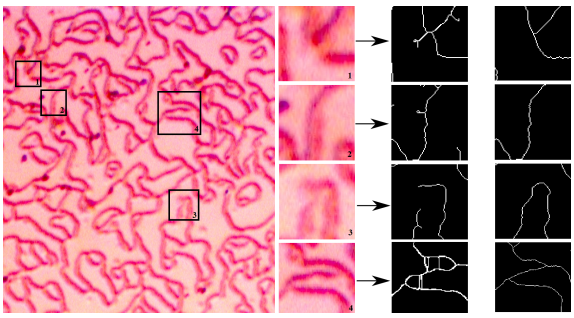

Figure 13: Errors of past methods in subareas of Figure 1. **1st**: extra edges (Zhang and Suen, 1984), **2nd**: extra degree 1 vertex (Guo and Hall, 1989), **3rd**: lost connection (Arganda-Carreras et al., 2010), **4th**: many superfluous edges (Delgado-Friedrichs et al., 2014). **Right**: our mesh.

We improve the erosion algorithm from section 4 by processing pixels not row by row, but in a data-driven recursive way starting from the external layer.

Definition 9. *For any binary image $I \subset \Omega$ consisting of black pixels on a white background $\Omega - I$, the* external layer *of I is the subset $L \subset I$ of all black pixels adjacent to a white pixel in the 4-connected grid.*

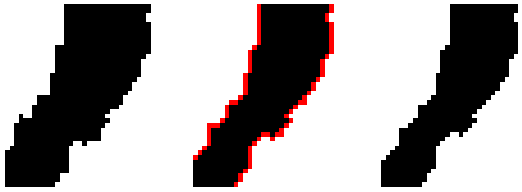

Figure 14: The red external layer from Def. 9 is removed.

A continuous deformation of the image domain Ω is any bijection $\Omega \to \Omega$ such that any adjacent pixels (in the 8-connected grid of Ω) map to adjacent pixels.

Corollary 10. *For any binary image $I \subset \Omega$, the symmetric thinning algorithm outputs a skeleton S that is invariant under any continuous deformation of Ω and satisfies the conclusions of Theorems 6 and 8. Any pixel of S has only 2 or 3 neighboring pixels in S.*

The symmetric skeletons obtained from all our microscopic images had no black 2×2 blocks, which were allowed in a 1-pixel wide skeleton from Definition 5. To guarantee that every skeleton has vertices of only degrees 2 or 3, the final step of Stage 2 after symmetric thinning is to resolve few cases of degree 4 vertices in Figure 15, which preserve connectivity in 5×5 or 6×6 neighborhood.

Proof of Corollary 10. The only difference between the erosion algorithm in section 4 and the new symmetric thinning in Figure 14 is the order in which pixels are processed. Since Definition 9 uses adjacency of pixels in the 4-connected grid, the output remains the same under any continuous deformation of Ω. The conclusion about 2 or 3 neighbors follows from resolving all degree 4 cases in Figure 15. □

The symmetric skeleton is better centered along darkest pixels, compare the first two pictures in Figure 13. The average intensity (over more than 100 images) of the symmetrically thinned skeleton has dropped from 142.95 to 122.77 in comparison with section 4. The conversion of a pixel-based skeleton into a polygonal mesh uses the 8-connected grid. To minimize the number of vertices according to the problem in section 1, final Stage 3 applies the Douglas-Peucker straightening (Douglas and Peucker, 1973) of polygonal edges.

6 Comparisons with past methods

We chose algorithms (Zhang and Suen, 1984), (Guo and Hall, 1989), (Arganda-Carreras et al., 2010), because they are offered by OpenCV and ImageJ, while (Delgado-Friedrichs et al., 2014), (Kamani et al., 2018) are most recent since 2015. The methods (Zhang and Suen, 1984), (Guo and Hall, 1989) are implemented in OpenCV and require a binary image as input, which can be produced by the original Otsu thresholding (also by OpenCV). The ablation study in Table 1 shows these thinning algorithms are substantially improved by our adaptive thresholding in section 3.

Figure 16 shows 6 example outputs on the image from Figure 1. The authors of (Arganda-Carreras et al., 2010) kindly distributed their software, which produced the 3rd skeleton in Figure 16. The 4th skeleton in Figure 16 was obtained by the code from the authors of the Morse-Smale skeleton (Delgado-Friedrichs et al., 2014). The authors of (Kamani et al., 2018) had provided their flux-based skeletonization code whose output is the 5th picture of Figure 16. The final picture of Figure 16 shows our mesh after Stage 3. In Figure 16 the past 5 methods either lost connectivity (ImageJ) or kept too many small loops (Delgado-Friedrichs et al., 2014) or superfluous hanging edges (Zhang and Suen, 1984), (Arganda-Carreras et al., 2010). The connectivity guarantees in (Guo and Hall, 1989, Proposition A.3) are too weak for microscopic images that need correct homotopy types for 1-pixel wide skeletons in Theorems 6, 8.

Table 1 shows the averages over more than 100 images. The Optimal Mesh Problem stated in section 1 required to minimize the average grayscale intensity over the mesh, because polygonal edges are

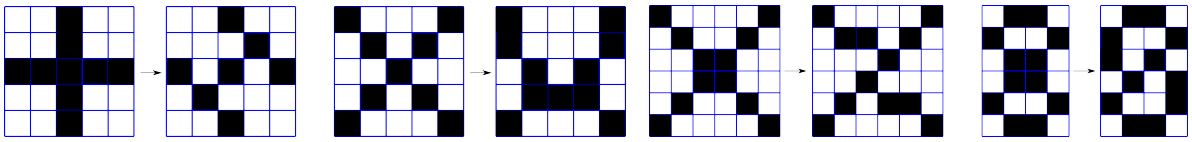

Figure 15: Resolving 2×2 black blocks and black pixels with 4 neighbors while preserving the local connectivity.

Figure 16: Output skeletons from past algorithms on the input image in Figure 1 from left to right: (Zhang and Suen, 1984), (Guo and Hall, 1989), (Arganda-Carreras et al., 2010), (Delgado-Friedrichs et al., 2014), (Kamani et al., 2018), ours.

expected to pass through darkest pixels. In addition to the average intensity, Table 1 includes the number of components, because a final skeleton should have one huge component and very few small ones.

The last column in Table 1 counts the total number of vertices including degree 2 vertices (bends of polygonal lines). The straightening of polygonal edges in Stage 3 substantially reduces these degree 2 vertices while the average intensity is only slightly increased to 130.2 and remained smaller than for all other past algorithms. If we remove small components in outputs of (Zhang and Suen, 1984), (Guo and Hall, 1989) so that their average numbers 177 and 112 of components drop, there will be hundreds (of 433 and 954 on average) degree 1 vertices in Figure 16.

In addition to Table 1, starting from 10 our outputs on real images, we have generated 625 times more synthetic ground truth images as follows:

- increased the thickness of skeletons by scaling each black pixel by a factor $k = 1,2,3,4,5$.
- applied Gaussian blur for kernel sizes $3,5,7,9,11$;
- added Gaussian noise with variances $1,2,3,4,5$;
- made 5%,10%,15%,20%,25% random pixels black.

Since (Arganda-Carreras et al., 2010) and (Delgado-Friedrichs et al., 2014) don't run for many images, Table 2 compares our meshes with the OpenCV algorithms (Zhang and Suen, 1984), (Guo and Hall, 1989) over 6250 synthetic images.

Pixels in the ground truth and output skeletons are

algorithms / quality measures	average intensity	connected components	deg 1 vertices	all vertices
Ground truth	123.7	3	0	819
(Zhang and Suen, 1984): original Otsu thresholding	135.3	956	1,577	13,927
(Zhang and Suen, 1984): thresholding from section 3	137.6	177	433	30,525
(Guo and Hall, 1989): original Otsu thresholding	135.7	966	2,417	12,129
(Guo and Hall, 1989): thresholding from section 3	130.8	112	954	29,927
(Kamani et al., 2018): original Otsu thresholding	156.7	5	2,653	25,364
(Kamani et al., 2018): thresholding from section 3	161.3	5	451	61,355
ImageJ (Arganda-Carreras et al., 2010)	139.2	52	268	30,462
Morse-Smale (Delgado-Friedrichs et al., 2014)	162.4	3	34	27,612
section 4: without symmetry	145.4	3	0	28,563
section 5: with symmetry	**126.7**	3	0	23,449
our output after straightening	**130.2**	3	0	**824**

Table 1: Objective comparison of 6 thinning algorithms (with variations) on more than 100 highly noisy real images.

considered *close* if they are in 3×3 neighborhoods of each other. The true positives (TP or hits) are pixels in the output close to ground truth. False positives (TP or false alarms) are the pixels in the output that are not close to the ground truth. The false negatives (FN or misses) are the pixels in the ground truth that are not close to the output. The accuracy measures in Table 2 are precision $= \frac{TP}{TP+FP}$, recall $= \frac{TP}{TP+FN}$ and F_1 score $= 2\frac{\text{precision} \times \text{recall}}{\text{precision} + \text{recall}}$.

algorithms	precision	recall	F_1 score
Zhang-Suen (Zhang and Suen, 1984)	0.068	0.862	0.126
Guo-Hall (Guo and Hall, 1989)	0.072	0.859	0.133
our method	0.933	0.963	0.948

Table 2: Accuracy over 6250 synthetic ground truths.

The complexity of the algorithm is linear in the number of pixels, because all steps in sections 3-5 involve small neighborhoods of pixels. The time is less than 1 sec per image on a laptop with 16GB RAM.

7 Discussion and conclusions

According to Table 1, the Morse-Smale complex (Delgado-Friedrichs et al., 2014) is closest to our vortex mesh in the total number of components and degree 1 vertices, but has the worst average intensity. The thinning algorithms (Zhang and Suen, 1984), (Guo and Hall, 1989) offered by OpenCV produce well-centered skeletons (close to our vortex meshes), but contain too many small components and degree 1 vertices that are not filtered out. The new thresholding in section 3 makes these skeletons better connected. The performance of AnalyzeSkeleton (Arganda-Carreras et al., 2010) is roughly between the Morse-Smale and OpenCV skeletons.

The deep learning papers (Asghari and Jalali, 2015), (Shen et al., 2017) provided their implementations and trained models. Since our images were not in their training data, these algorithms performed poorly on microscopic images because of the intensity variations and noise. An extended version will include these outputs on images similar to Figure 1.

• The new erosion algorithm in section 4 guarantees a 1-pixel wide skeleton with a correct homotopy type (stronger than a graph connectivity) by Theorems 6 and 8. The erosion rules are simpler than those in (Zhang and Suen, 1984) and (Guo and Hall, 1989).

• The first 6 rows of Table 1 show that the new adap-

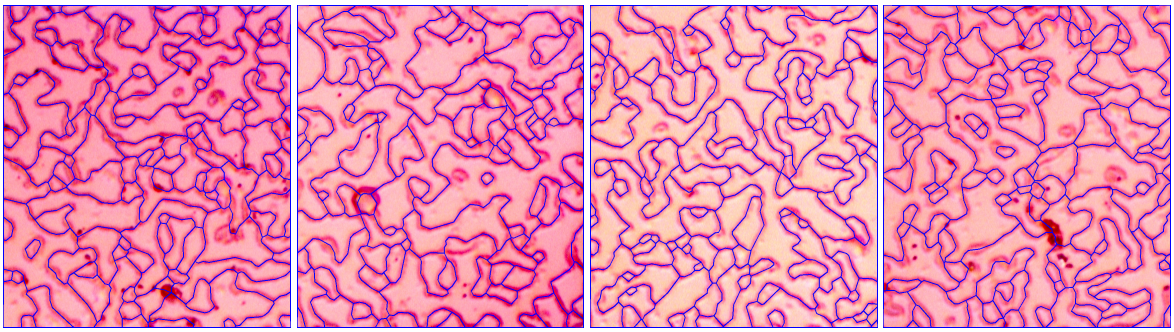

Figure 17: Our final polygonal meshes on more challenging microscopic images with high noise.

tive thresholding in section 3 improves the continuity of past skeletons by reducing degree 1 vertices.

• The new symmetric thinning in section 5 outperforms the past thinning by reducing the average intensity over the mesh to 126.7, which goes up only slightly after straightening polygonal lines.

• Tables 1, 2 and Figures 17, 18 show that our mesh is robust under high noise and has better accuracy in comparison with several past algorithms on more than 100 real and 6250 ground truth images.

REFERENCES

Arganda-Carreras, I., Fernández-González, R., Muñoz-Barrutia, A., and Ortiz-De-Solorzano, C. (2010). 3d reconstruction of histological sections: application to mammary gland tissue. *Microscopy Res. & Tech.*, 73:1019–1029.

Asghari, M. H. and Jalali, B. (2015). Edge detection in digital images using dispersive phase stretch transform. *International journal of biomedical imaging*.

Bernard, T. M. and Manzanera, A. (1999). Improved low complexity fully parallel thinning algorithm. In *Proc. Image Analysis and Processing*, pages 215–220.

Bernsen, J. (1986). Dynamic thresholding of gray-level images. In *Proc. Intern. Conf. Pattern Recognition*.

Canny, J. (1986). A computational approach to edge detection. *Transactions PAMI*, 6:679–698.

Delgado-Friedrichs, O., Robins, V., and Sheppard, A. (2014). Skeletonization and partitioning of digital images using discrete morse theory. *Trans. Pattern Analysis and Machine Intelligence*, 37(3):654–666.

Douglas, D. and Peucker, T. (1973). Algorithms for the reduction of the number of points required to represent a digitized line or its caricature. *Cartographica*, 10(2):112–122.

Guo, Z. and Hall, R. W. (1989). Parallel thinning with two-subiteration algorithms. *Comm. ACM*, 32(3):359–373.

Kalisnik, S., Kurlin, V., and Lesnik, D. (2019). A higher-dimensional homologically persistent skeleton. *Advances in Applied Mathematics*, 102:113–142.

Kamani, M., Farhat, F., Wistar, S., and Wang, J. (2018). Skeleton matching with applications in severe weather detection. *Appl. Soft Computing*, 70:1154–1166.

Kurlin, V. (2014a). Auto-completion of contours in sketches, maps and sparse 2d images based on topological persistence. In *Proceedings of CTIC: Computational Topology in Image Context*, pages 594–601.

Kurlin, V. (2014b). A fast and robust algorithm to count topologically persistent holes in noisy clouds. In *Proc. Computer Vision Pattern Recogn.*, pages 1458–1463.

Kurlin, V. (2015a). A homologically persistent skeleton is a fast and robust descriptor of interest points in 2d images. In *Proceedings of CAIP*, pages 606–617.

Kurlin, V. (2015b). A one-dimensional homologically persistent skeleton of an unstructured point cloud. In *Comp. Graphics Forum*, volume 34, pages 253–262.

Kurlin, V. (2016). A fast persistence-based segmentation of noisy 2d clouds with provable guarantees. *Pattern Recognition Letters*, 83:3–12.

Lin, S.-Z., Wang, X., Kamiya, Y., Chern, G.-W., Fan, F., Fan, D., Casas, B., Liu, Y., Kiryukhin, V., Zurek, W. H., and Cheong, S.-W. (2014). Topological defects as relics of emergent continuous symmetry and higgs condensation of disorder in ferroelectrics. *Nature Physics*, 10(12):970.

Niblack, W. (1985). *An introduction to digital image processing*. Strandberg Publishing Company.

Otsu, N. (1979). A threshold selection method from gray-level histograms. *IEEE transactions on systems, man, and cybernetics*, 9(1):62–66.

Panichev, O. and Voloshyna, A. (2019). U-net based convolutional neural network for skeleton extraction. In *Proceedings of the CVPR workshops*.

Phansalkar, N., More, S., Sabale, A., and Joshi, M. (2011). Adaptive local thresholding for detection of nuclei in diversity stained cytology images. In *Intern. Conf. Comm. and Signal Processing*, pages 218–220.

Saha, P. K., Borgefors, G., and di Baja, G. S. (2016). A survey on skeletonization algorithms and their applications. *Pattern Recognition Letters*, 76:3–12.

Sauvola, J. and Pietikäinen, M. (2000). Adaptive document image binarization. *Pattern Recogn.*, 33(2):225–236.

Shen, W., Zhao, K., Jiang, Y., Wang, Y., Bai, X., and Yuille, A. (2017). Deepskeleton: Learning multi-task scale-associated deep side outputs for object skeleton ex-

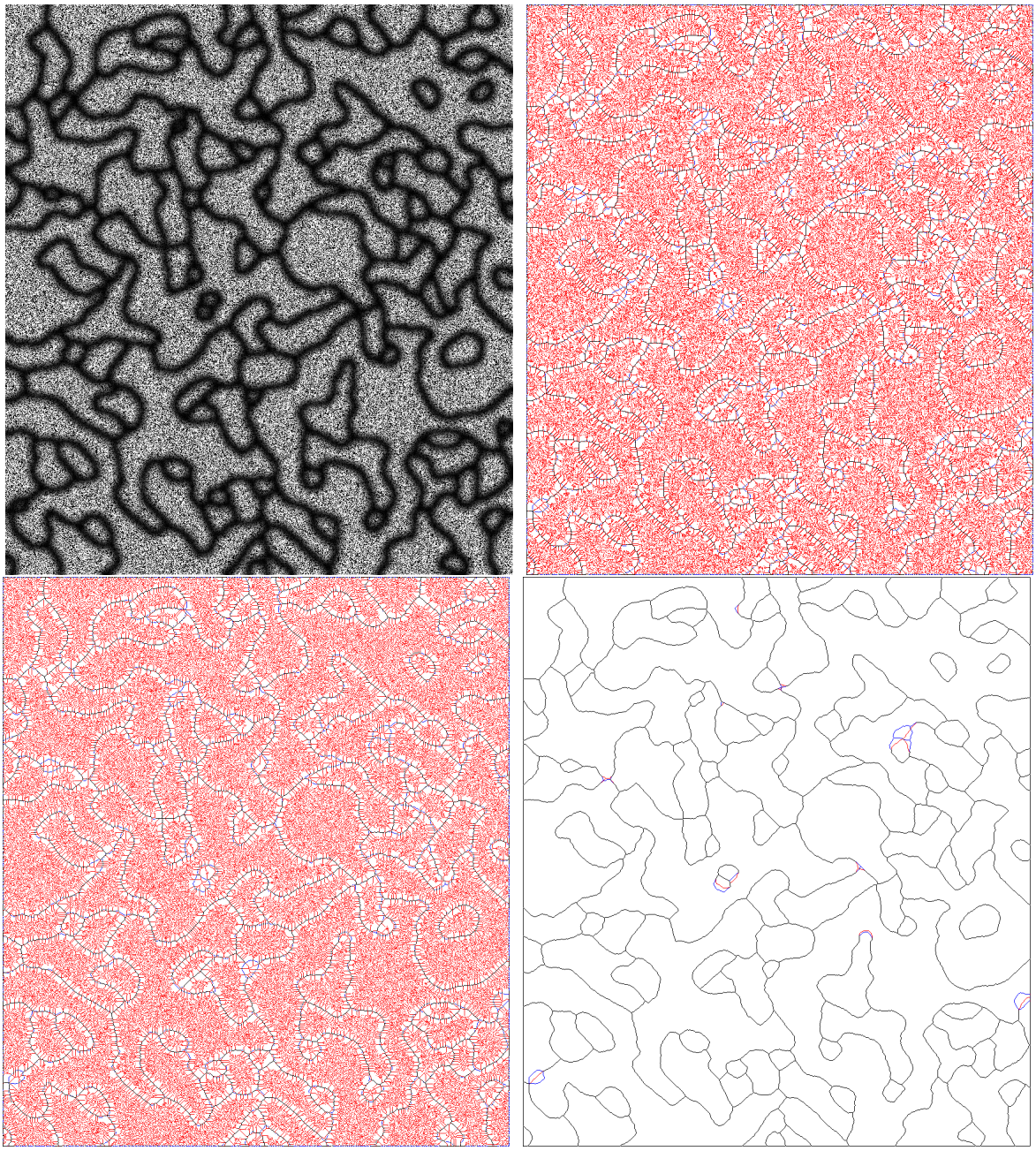

Figure 18: **1st:** one of 6250 synthetic images with noise over a ground truth skeleton (easy to skeletonize for humans), **2nd:** (Zhang and Suen, 1984), **3rd:** (Guo and Hall, 1989), **4th:** our output. True Positives are black. False Positives are red. False Negatives are blue. The OpenCV algorithms (Zhang and Suen, 1984), (Guo and Hall, 1989) output too many false positives.

traction in natural images. *IEEE Transactions on Image Processing*, 26(11):5298–5311.

Smith, P. and Kurlin, V. (2019). Skeletonisation algorithms with theoretical guarantees for unorganised point clouds with high levels of noise. *arXiv:1901.03319*.

Soille, P. (2013). *Morphological image analysis: principles and applications*. Springer Science & Business.

Soille, P. and Vincent, L. (1990). Determining watersheds in digital pictures via flooding simulations. In *Visual Comm. Image Proc.*, volume 1360, pages 240–250.

Wang, Y., Xu, Y., Tsogkas, S., Bai, X., Dickinson, S., and Siddiqi, K. (2018). Deepflux for skeletons in the wild. *arXiv:1811.12608*.

Zhang, T. and Suen, C. Y. (1984). A fast parallel algorithm for thinning digital patterns. *Communications of the ACM*, 27(3):236–239.